

Analysis of Hydrogen Tunneling in an Enzyme Active Site Using von Neumann Measurements

Isaiah Sumner and Srinivasan S. Iyengar*

*Department of Chemistry and Department of Physics, Indiana University,
800 E. Kirkwood Ave, Bloomington, Indiana 47405*

Received November 25, 2009

Abstract: We build on our earlier quantum wavepacket study of hydrogen transfer in the biological enzyme soybean lipoxygenase-1 by using von Neumann quantum measurement theory to gain qualitative insights into the transfer event. We treat the enzyme active site as a measurement device which acts on the tunneling hydrogen nucleus via the potential it exerts at each configuration. A series of changing active site geometries during the tunneling process effects a sequential projection of the initial, reactant state onto the final, product state. We study this process using several different kinds of von Neumann measurements and show how a discrete sequence of such measurements not only progressively increases the projection of the hydrogen nuclear wavepacket onto the product side but also favors proton over deuterium transfer. Several qualitative features of the hydrogen tunneling problem found in wavepacket dynamics studies are also recovered here. These include the shift in the “transition state” toward the reactant as a result of nuclear quantization, greater participation of excited states in the case of deuterium, and the presence of critical points along the reaction coordinate that facilitate hydrogen and deuterium transfer and coincide with surface crossings. To further “tailor” the dynamics, we construct a perturbation to the sequence of measurements, that is a perturbation to the dynamical sequence of active site geometry evolution, which leads us to insight on the existence of sensitive regions of the reaction profile where subtle changes to the dynamics of the active site can have an effect on the hydrogen and deuterium transfer process.

I. Introduction

Hydrogen transfer reactions^{1–3} play a significant role in many organic^{2–5} and biological^{6–10} reactions. Due to the de Broglie wavelength of the transferring hydrogen atom, the role of quantum nuclear effects in such reactions has been one focus area of study.^{2–27} Experimentally, an important indication of quantum nuclear effects including tunneling is the appearance of an unexpectedly large primary kinetic isotope effect (KIE), which has been noted in many lipoxygenases. For example, the room temperature rate constant for hydrogen nuclear transfer (k_H) catalyzed by the enzyme soybean lipoxygenase-1 (SLO-1)^{13,16–18,23–26,28–32} is a factor of 81 larger than that for deuterium nuclear transfer (k_D).²⁹ Human lipoxygenase was noted to have a similar behavior.³³ Quantum mechanical tunneling has been proposed to have

a central role in this phenomenon,^{16,23,24,26} since this observation cannot be explained using classical rate theories. Temperature dependence of primary and secondary isotope effects is another set of experimentally measurable parameters that directly probe the extent of quantum nuclear effects. The proper description of nuclear quantum effects for hydrogen-transfer reactions, including the role of tunneling, is a challenging and an often actively debated area of study.^{6,9,10,19,22,27,34–36}

A few of the approaches that adequately treat the quantum nuclear effect and have been used to study hydrogen transfer in enzymes are as follows. [This paragraph is not an exhaustive review of all treatments of quantum nuclear effects in enzymes but only highlights some of the prevailing studies. For a detailed overview of the methods employed, see refs 6, 7, 9, 10, and 22 and publications cited within these references.] Klinman and co-workers experimentally¹¹

* Corresponding author e-mail: iyengar@indiana.edu.

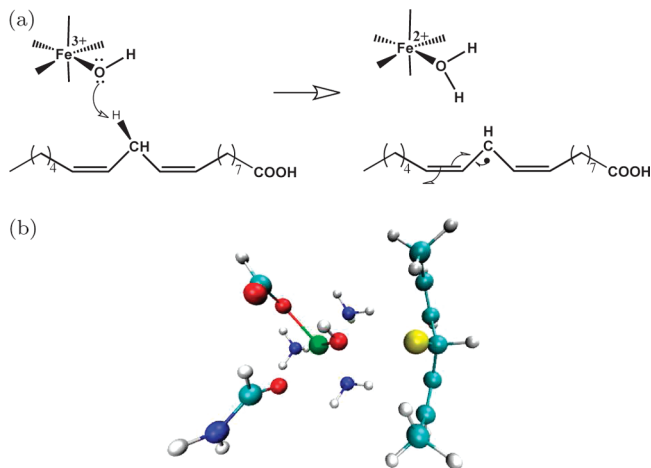


Figure 1. (a) The rate-determining step in SLO-1 and (b) one of the two active site models used in ref 26 with pruned representations of the active site residues and the substrate. The transferring hydrogen is enlarged and shown in yellow.

noted the effect of tunneling on the hydrogen transfer steps in biological enzyme catalysis. They have subsequently computed associated rates with a vibrationally nonadiabatic methodology^{37,38} that employs Franck–Condon-like overlaps based on one-dimensional potentials. Warshel and co-workers^{14–17,36} used Feynman path integral approaches^{39–41} to describe the trajectory of the quantized hydrogen nucleus, which moves on an enzyme potential surface computed from empirical valence bond (EVB) theory.^{7,42–44} Additionally, calculations on the uncatalyzed reaction in a reference solution [usually water] allowed them to explore enzyme-specific contributions to catalysis.^{16–21} Truhlar, Gao and co-workers^{22,32} have utilized a multidimensional tunneling correction to variational transition state theory,^{22,34} where the potential energy surfaces are generally obtained from QM/MM calculations.^{45–48} Hammes-Schiffer and co-workers^{23,49} implemented a vibronically nonadiabatic formalism to treat proton-coupled electron transfers. This method is based on EVB^{7,42–44} and includes quantum mechanical treatment of one electron and one proton that undergo proton-coupled electron transfer. The protein is treated through classical molecular dynamics simulations.^{7,42–44} Schwartz and co-workers¹⁰ utilized a semiclassical description based on the Langevin equation. A classical dynamics simulation was conducted with a Hamiltonian that includes parametrized, analytical potentials and environmental interactions. The trajectory determined a friction kernel, which was used to calculate the quantum mechanical rate constant using the flux operator formalism.⁵⁰ Siebrand and Smedarchina²⁵ applied time-dependent perturbation theory with a one-dimensional potential surface.

In a recent publication,²⁶ we explored the hydrogen and deuterium nuclear tunneling process involved in the rate-determining step in the catalytic cycle of the enzyme SLO-1. This step [see Figure 1a] involves the abstraction of a hydrogen atom from the substrate [linoleic acid] by the octahedral Fe^{3+} -OH complex present deep in the active site.^{13,16,17,23–25,28–31} The reaction displays a large KIE [$k_{\text{H}}/k_{\text{D}}$] of 81 at room temperature under certain mutations.²⁹ In ref 26, we computed the hydrogen tunneling probabilities for a model system constructed from the active site atoms

in close proximity to the iron cofactor in SLO-1 [Figure 1b]. This simplification of the active site is based on the assumption that only the immediate environment exerts an electronic influence on the hydrogen nuclear transfer. We described the tunneling hydrogen nucleus [proton or deuteron] as a three-dimensional quantum wavepacket^{26,51–55} coupled to the change in electronic structure which was computed using hybrid density functional theory, benchmarked with MP2 post-Hartree–Fock theory. At each step of the quantum dynamics, the potential surface was computed by including all electrons in our model system. As a result, our method is not restricted to a specific mode of transfer such as proton coupled electron transfer,^{23,24} proton transfer, hydrogen transfer, or hydride transfer. Also, since the transferring nuclear wavepacket is propagated via the time-dependent Schrödinger equation, using an efficient and accurate “distributed approximating functional” propagator,^{26,51,52,56,57} all quantum effects pertaining to the quantized H/D nucleus as well as those arising from the electronic degrees of freedom within the model are included. However, it must be noted that the main goal of ref 26 was to evaluate the quantum nuclear contribution to the hydrogen transfer step. This aspect was studied through rigorous quantum dynamics conducted on surfaces created from electronic structure theory. Hence, the exact nature of large-scale rearrangements of the protein that may facilitate gating modes and the contribution of nuclear quantum effects to catalysis were not explicitly probed. Therefore, only reduced active site models [such as in Figure 1a] were considered. Similar models have been used in previous studies on metalloenzymes.^{31,58}

The kinetic isotope effect was computed using the transmission amplitude of the wavepacket, and the experimental value was reproduced. Some physical insights gleaned from our studies in ref 26 are as follows: (a) Tunneling for both hydrogen and deuterium occurs through the existence of distorted, spherical “s”-type hydrogen nuclear wavefunctions and “p”-type polarized hydrogen nuclear wavefunctions for transfer along the donor–acceptor axis. (b) There is also a significant population transfer through distorted “p”-type hydrogen nuclear wavefunctions directed perpendicular to the donor–acceptor axis [via intervening “ π ”-type interactions] which underlines the three-dimensional nature of the tunneling process. The quantum dynamical evolution indicates a significant contribution from tunneling processes both along the donor–acceptor axis and along directions perpendicular to the donor–acceptor axis. (c) The hydrogen nuclear wavefunctions display curve-crossings, in a fashion similar to electronic states. The tunneling process is vibrationally nonadiabatic and is facilitated by these curve-crossings. In our calculations, multiple proton and deuteron excited states (greater than five) were shown to contribute to tunneling. (d) The inclusion of nuclear quantization shifted the transition-state toward the reactants. The precise location of the shifted transition state, however, depends on the populations of each hydrogen and deuterium eigenstate during dynamics.²⁶

In this publication, we inspect the hydrogen transfer problem in SLO-1 using the concept of measurement-driven

quantum evolution. The enzyme active site is treated as a measurement device. The effect it has on the hydrogen transfer process is represented using the potential energy surfaces computed in ref 26. Thus, while the enzyme active site is not included in an atomistic fashion, its effect is accounted for as stated above. We use this analysis to probe whether the action of the enzyme active site during the hydrogen transfer step of the catalysis process can be described using a measurement paradigm. As we find here, these ideas have utility in providing a qualitative description of the hydrogen transfer step, and we find that such a measurement can accelerate the hydrogen nuclear transfer process as compared to the deuterium transfer process. However, a detailed quantitative description requires the use of quantum dynamics, such as that performed in ref 26. It is important to note that this study focuses on the hydrogen transfer step and hence cannot elucidate the role of measurement on the overall catalytic process.

To facilitate the discussion, we provide a brief overview of the basic ideas of measurement in section II. As will become clear, the mathematical formalisms presented are influenced by those utilized in the fields of quantum information theory and optimal control.^{59–61} In this section, we also outline a set of measurement criteria that are used later in section III to make connections to the proton transfer event in SLO-1. In section III, we consider alterations to the measurement and active site atomic evolution sequence to tailor the H/D transfer probability. Conclusions are presented in section IV.

II. Measurement-Induced Control of Quantum Processes

In quantum theory, measuring a system can fundamentally alter its state. Perhaps the most familiar examples of this phenomenon are the sequential Stern-Gerlach experiments, which measure the spin of silver atoms.⁶² The Stern-Gerlach experiments pertain to population transfer between $|S_z^\pm\rangle$ spinor states through the application of an external magnetic field. As an illustrative example, suppose an ensemble of atoms was prepared that only had the “spin down” component along the z axis, i.e., $|S_z^-\rangle$. Next, these atoms are subjected to a magnetic field along the x or y directions, which leads to a “spin measurement.” If the spin along the z axis were again measured, through application of a magnetic field along the z axis, half of the atoms would be spin down, $|S_z^-\rangle$, like our original system, but the other half would now be spin up, $|S_z^+\rangle$. In other words, the intermediate measurement projected [or altered] the state of the original system such that half of the $|S_z^-\rangle$ population is now in a different, orthogonal state, $|S_z^+\rangle$. Generally, a Stern-Gerlach experiment is treated as an instantaneous, von Neumann measurement.⁶³

In a von Neumann measurement, the initial state is projected onto the eigenstates of the measurement operator. If the outcome of the measurement is recorded, the wavefunction collapses onto a specific measurement operator eigenstate, like $|S_z^+\rangle$ in the Stern-Gerlach example. von Neumann measurements have been used in studies detailing how quantum measurements can drive an initial system to a specific set of target states which are orthogonal to the

original state.^{59,64–68} A quantum system coupled to a classical system or bath can also be interpreted as a quantum measurement process.^{59,69–75} [This perspective can be rationalized with the Stern-Gerlach example as well, since the Stern-Gerlach magnet (measurement device) is treated as a classical object, whereas the silver atom spin states are quantum-mechanical.] It is these two properties of quantum measurement theory that we exploit in this study.

We inspect the hydrogen transfer in SLO-1, by invoking the idea that the initial state of the hydrogen nucleus [the donor state] is driven to a final, orthogonal acceptor state [or a finite set of acceptor states] by a series of measurements. Here, the active site in SLO-1, treated as a classical system, constructs a series of measurements on the hydrogen nucleus, a quantum system. Furthermore, our results indicate that the series of measurements enacted by SLO-1 along the reaction path accelerate proton transfer over deuteron transfer. We explore three types of von Neumann measurements, which are described in the following subsections. This tiered set spans a wide range of perceivable measurement-induced perturbations of the quantized hydrogen nucleus due to the active site atoms. They differ from each other and from standard unitary evolution through the discrete elimination of off-diagonal matrix elements or coherences of the density matrix.

In other words, let us first consider the time-evolution of a wavepacket $|\chi(t)\rangle = U(t)|\chi(0)\rangle$, or the density matrix, $U(t)\rho_0U(t)^\dagger$, where $U(t)$ is the time-evolution operator appropriate for a reduced-dimensional Hamiltonian, $H(t)$, which depends on an effective time-variable, t . In ref 26, $H(t) = -(\hbar^2/2m_H)\nabla_{R_H}^2 + V^{\text{DFT}}(R_H; \{\mathbf{R}_{\text{as}}\}; t)$, where R_H represents the position of the tunneling proton or deuteron and $V^{\text{DFT}}(R_H; \{\mathbf{R}_{\text{as}}\}; t)$ is the density-functional potential at R_H , that also depends on the active site geometry, \mathbf{R}_{as} , as seen in Figure 3. It is important to note that, when the Hamiltonian is time-independent, the projected probability of a propagated wavepacket onto a final state, $|\langle f|\chi(t)\rangle|^2$, is generally an oscillatory (periodic) function of time. The periodic nature is defeated to obtain a nearly monotonic form of such a final state projection in ref 26 through the time-dependence of the reduced dimensional Hamiltonian. We treated the tunneling phenomenon in SLO-1 in ref 26 using (a) unitary propagation of a wavepacket on potentials described by the local geometry of the enzyme active site and (b) adaptation of the propagator to the change in the active site geometry. However, as we will see in the next subsections, a similar qualitative effect on the projected probabilities can also be achieved through a measurement operator paradigm, where the measurement operators are determined from the active site geometries and induce H-transfer. Although this type of measurement-induced control has also been analyzed by others^{67,68} by including unitary propagation interspersed between a finite number of measurements, in the current publication, we aim to study the effect of measurement [i.e., the active site evolution] alone on the H/D transfer phenomenon.

A. Filtered Measurements. Consider a Hilbert space comprised of the orthogonal kets $\{|D\rangle; |A_m\rangle\}$, where m enumerates the kets comprising a N_A -dimensional subspace. In addition, let $|D\rangle$ denote the initial state of the system, or

more generally, $\rho_0 \equiv |D\rangle\langle D|$, and let $\{|A_m\rangle\}$ be the target subspace. In the case of SLO-1, $|D\rangle$ may be regarded as the donor state for the transferring proton wavefunction, whereas $\{|A_m\rangle\}$ is a set of acceptor states. [Note that, while we consider only one $|D\rangle$ state, the treatment is easily generalized.] We wish to drive the $|D\rangle$ state population to the $\{|A_m\rangle\}$ subspace via a series of intermediate measurements, $\{\hat{\mathcal{M}}_I\}$. Thus, the measurements in some sense take the role of active site motions. In the next section, we make this connection more explicit. The dyadic representation of the intermediate measurement operators is $\hat{\mathcal{M}}_I = \sum_j^{N_{DM}(I)} M_j^I |M_j^I\rangle\langle M_j^I| = \sum_j M_j^I P_j^I$, where $\{M_j^I\}$ and $\{|M_j^I\rangle\}$ are the eigenvalues and eigenvectors of $\hat{\mathcal{M}}_I$, $N_{DM}(I)$ is the dimensionality of the I th measurement space, and P_j^I is the j th projector of the I th measurement operator. The projectors resolve the identity, i.e., $\sum_j P_j^I = \mathbf{I}$, where \mathbf{I} is the identity matrix, and are idempotent, i.e., $P_j^I P_k^I = \delta_{j,k} P_j^I$, where $\delta_{j,k}$ is the Kronecker delta. However, for two sets of measurements, $I \neq J$, $P_j^I P_k^J = \langle M_j^I | M_k^J \rangle |M_j^I\rangle\langle M_k^J|$, where $\langle M_j^I | M_k^J \rangle$ is not necessarily $\delta_{j,k}$. That is, the measurement operators do not commute with each other in general and do not have simultaneous eigenstates.

In a filtered measurement scheme, which is also referred to as a selective measurement scheme,⁶⁷ the original state, represented as the density matrix ρ_0 , is measured by $\hat{\mathcal{M}}_I$, resulting in a new state $\rho_I = \sum_j^{N_{DM}} P_j^I \rho_0 P_j^I$. [To simplify the notation, we have chosen to drop the dependence of N_{DM} on the measurement operator, I .] The $|D\rangle$ and $\{|A_m\rangle\}$ populations of ρ_I are then also observed, i.e., measured. Filtered measurements have been studied for possible use in the field of quantum computation.⁶⁴ The probability of finding the system in the $\{|A_m\rangle\}$ subspace after the measurement $\hat{\mathcal{M}}_I$ on ρ_0 is

$$\sum_m^N \sum_j^{N_{DM}} \langle A_m | P_j^I | D \rangle \langle D | P_j^I | A_m \rangle = \sum_m^N \sum_j^{N_{DM}} |\langle A_m | M_j^I \rangle \langle M_j^I | D \rangle|^2 \quad (1)$$

Thus, the probability density not in $\{|A_m\rangle\}$, i.e., the probability density remaining in $|D\rangle$, is

$$1 - \sum_m^N \sum_j^{N_{DM}} |\langle A_m | M_j^I \rangle \langle M_j^I | D \rangle|^2 \quad (2)$$

If the net probability in eq 2 is nonzero, additional measurements may further drive the population from $|D\rangle$ to $\{|A_m\rangle\}$. After a sequence of N_I such measurements, the accumulated probability in the $\{|A_m\rangle\}$ subspace is given by⁶⁴

$$\left\{ 1 - \prod_{I=1}^{N_I} \left[1 - \sum_m^N \sum_j^{N_{DM}} |\langle A_m | M_j^I \rangle \langle M_j^I | D \rangle|^2 \right] \right\} \quad (3)$$

For the special case of a two-dimensional Hilbert space, comprised of $\{|D\rangle; |A\rangle\}$, eq 3 reduces to

$$\left\{ 1 - \prod_{I=1}^{N_I} \left[1 - \sum_{j=1}^2 |\langle A | M_j^I \rangle \langle M_j^I | D \rangle|^2 \right] \right\} = \left\{ 1 - \prod_{I=1}^{N_I} \left[1 - \frac{1}{2} \sin^2 2\theta_I \right] \right\} \quad (4)$$

where $\langle M_1^I | D \rangle \equiv \cos \theta_I$. In further discussions, we refer to this process as a “filtered measurement” process since the component of the state in the $\{|A_m\rangle\}$ subspace is filtered out at each measurement step [eq 2], and therefore, probability only moves in the forward, $|D\rangle \rightarrow \{|A_m\rangle\}$, direction. This is the case, for example, in chemical reactions where the products, once formed, are not available for back-reaction. [A similar process, described by a different realization of measurement theory, is presented in ref 69.] This point becomes clear when one understands eq 1 to be a discrete path integral in Hilbert space that contains only $|D\rangle \rightarrow \{|M_j^I\rangle\} \rightarrow \{|A_m\rangle\}$ paths. Therefore, if a measurement drives $|D\rangle$ to $\{|A_m\rangle\}$, the transfer is complete and further measurements cause no change.

B. Unfiltered Measurements. Unlike the filtered measurement process discussed in the previous section, the “unfiltered measurement”, or nonselective measurement process,⁶⁷ does not subject the system to a $\{|D\rangle; |A_m\rangle\}$ interrogation after each intermediate measurement. The consequences of this distinction will be explained in the sections below, where we discuss two separate kinds of “unfiltered measurements”. The “complete space unfiltered measurement” process is discussed in section II.B.1, and the “reduced space unfiltered measurement” process is discussed in section II.B.2.

1. Complete Space. In the complete space, unfiltered measurement formalism, we represent the system's state after a measurement $\hat{\mathcal{M}}_I$ on ρ_0 as the density matrix

$$\rho_I = \sum_j P_j^I \rho_0 P_j^I = \sum_j |\langle M_j^I | D \rangle|^2 |M_j^I\rangle\langle M_j^I| = \sum_j \rho_j^I P_j^I \quad (5)$$

where ρ_j^I is the probability associated with state $|M_j^I\rangle$. It is convenient, but not necessary, to express the density matrix in the basis of the eigenstates of the measurement operator, $\hat{\mathcal{M}}_I$. However, we no longer enforce a $\{|D\rangle; |A_m\rangle\}$ interrogation in ρ_I , as done in eq 1 of section II.A. The use of unfiltered measurements as an augmentation to optimal control experiments has been studied.⁵⁹ Using this notation, it can be shown^{59,67} that the result of a sequence of such unfiltered measurements acting on a system is calculated from the recursion relation

$$\rho_{I+1} = \sum_j^{N_{DM}} P_{I+1}^j \rho_I P_{I+1}^j = \sum_{j,i}^{N_{DM}} \rho_i^I |\langle M_j^{I+1} | M_i^I \rangle|^2 P_{I+1}^j \quad (6)$$

After N_I such measurements, the population in the $\{|A_m\rangle\}$ subspace is a discrete sum over paths of the form

$$\sum_m^N \langle A_m | \rho_{N_I} | A_m \rangle = \sum_m^N \sum_{j_1, j_2, \dots, j_{N_I}}^{N_{DM}} |\langle A_m | M_{j_{N_I}}^{N_I} \rangle \dots \langle M_{j_3}^{N_I} | M_{j_2}^{N_I} \rangle \langle M_{j_2}^{N_I} | M_{j_1}^{N_I} \rangle \langle M_{j_1}^{N_I} | D \rangle|^2 \quad (7)$$

The above, discrete path integral formalism reflects that all possible paths from $|D\rangle$ to $\{|A_m\rangle\}$ are allowed. Thus, unlike the filtered process in section II.A, the probability is not constrained to flow in one direction in the $\{|D\rangle; |A_m\rangle\}$ space. Thus, unfiltered measurements share characteristics of mi-

croscopic reversibility in chemical reactions. This distinction is more explicit if we rewrite the previous equation and only consider two intermediate measurements for simplicity. The summand in eq 7 now takes the form

$$\begin{aligned} & |\langle A_m | M_{j_2}^2 \rangle \langle M_{j_2}^2 | M_{j_1}^1 \rangle \langle M_{j_1}^1 | D \rangle|^2 = \\ & |\langle A_m | M_{j_2}^2 \rangle \langle M_{j_2}^2 | D \rangle \langle D | M_{j_1}^1 \rangle \langle M_{j_1}^1 | D \rangle + \\ & \langle A_m | M_{j_2}^2 \rangle \langle M_{j_2}^2 | \hat{\mathcal{R}} | M_{j_1}^1 \rangle \langle M_{j_1}^1 | D \rangle|^2 \end{aligned} \quad (8)$$

where $\hat{\mathcal{R}} = \mathbb{I} - |D\rangle\langle D|$. The first term in eq 8 contains $|D\rangle \rightarrow |D\rangle$ flow arising from the action of $|M_{j_1}^1\rangle$. Also, a comparison of eqs 7 and 3 reveals that the order of the measurements is only significant in the unfiltered scheme, since the $\{|D\rangle; |A_m\rangle\}$ filter in the operation described in section II.A disconnects one measurement from the next.

In the current scenario, all measurement eigenstates are explicitly observed. In the following section, we describe a process in which only a portion of the measurement space is observed.

2. Reduced Space. In the second unfiltered measurement procedure, the result of a sequence of measurements is obtained from the recursion relation^{59,67}

$$\begin{aligned} \rho_{I+1} = & \left[\sum_{\{k[I+1]\}} (P_{I+1}^{k[I+1]} \rho_I P_{I+1}^{k[I+1]}) \right] + \\ & \left(\mathbb{I} - \sum_{\{k[I+1]\}} P_{I+1}^{k[I+1]} \right) \rho_I \left(\mathbb{I} - \sum_{\{k[I+1]\}} P_{I+1}^{k[I+1]} \right) \end{aligned} \quad (9)$$

Here, the first summation is over the elements in the chosen $\{P_{I+1}^{k[I+1]}\}$ subspace, the elements of which may depend on the measurement index I . Notice further that, while this process does not allow off-diagonal blocks, i.e., $P_{I+1}^{k[I+1]} \rho_{I+1} [\mathbb{I} - P_{I+1}^{k[I+1]}] = 0$, ρ_{I+1} is not necessarily diagonal inside the $[\mathbb{I} - P_{I+1}^{k[I+1]}]$ subspace, as noted by the second term in eq 9. This is an important distinction between the two “unfiltered measurement” processes considered here. In the scheme described in section II.B.1, all off-diagonal elements of ρ in the measurement space are completely eliminated, since all eigenstates are explicitly measured. In this case only the $P_{I+1}^{k[I+1]}$ subspace is explicitly monitored. The remaining projectors are present in the orthogonal complement, $[\mathbb{I} - \sum_{\{k[I+1]\}} P_{I+1}^{k[I+1]}]$, and the density matrix is no longer diagonal inside the $\{|M_i^j\rangle\}$ basis [compare eqs 5 and 9.] Like the complete, unfiltered formalism described in section II.B.1, probability flow in the $\{|D\rangle; |A_m\rangle\}$ space is unrestricted. This process creates the $|D\rangle \rightarrow \{|A_m\rangle\}$ flow by measuring only the $\{k[I]\}$ subspace. Thus, it can be seen as a probe of the effectiveness of the $\{k[I]\}$ subspace to effect a measurement-induced population transfer.

A few comments are now in order with respect to the different measurement techniques discussed above. Let us start with the case where an intermediate set of operators $\{\hat{\mathcal{N}}_I\}$ exists, but at each stage there is no measurement process. In other words, $\rho_{I+1} = \sum_{i,j} \rho_{i,j}^{I+1} |M_i^{I+1}\rangle\langle M_j^{I+1}| = (\sum_i |M_i^{I+1}\rangle\langle M_i^{I+1}|) \rho_I (\sum_j |M_j^{I+1}\rangle\langle M_j^{I+1}|)$, and all off-diagonal elements in the measurement operator basis are retained at each stage. This is not a measurement and, in fact, will not evolve ρ_I , since $\sum_i |M_i^{I+1}\rangle\langle M_i^{I+1}| = \mathbb{I}$. This can be distinguished from the case discussed in section II.B.2, where some of the coherences are eliminated through the measure-

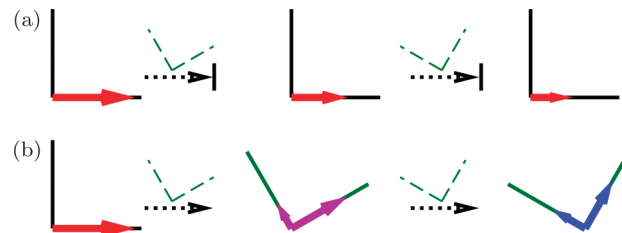


Figure 2. Illustration of filtered (a) and unfiltered (b) measurements. The initial density matrix population is shown using a red, horizontal arrow. The measurements are represented by the horizontal, dotted arrows and the eigenstates of the measurement operators are shown using dark green, dashed lines above these arrows. For example, the eigenstates of the first measurement are oriented at 30° and 120°, while those for the second are oriented at 60° and 150°. The vertical line after the arrow in (a) is the $\{|D\rangle; |A_m\rangle\}$ filter, which removes the vertical, $|A\rangle\langle A|$ component and repopulates the $|D\rangle\langle D|$ dyad. In the unfiltered case, the measurements populate the measurement eigenstates [eq 7], as can be seen from the purple and blue arrows in part (b). The population driven to the $|A\rangle\langle A|$ dyad after both measurements is 0.61 for (a) and 0.56 for (b). [This set of measurements is optimal for (b), as discussed in section III.C.2, whereas the optimal measurement for (a) should be taken at 45° each time.⁶⁴]

ment of a restricted subspace, whereas in section II.B.1, all of the coherences are eliminated. Finally, in section II.A, the process above is further enhanced by an additional measurement or interrogation of the system in the $\{|D\rangle; |A_m\rangle\}$ subspace. These measurements are pictorially represented in Figure 2. A Bloch vector formalism based on the Feynman–Vernon–Hellwarth theory of interaction with strong fields can also be used to depict this within a two-dimensional Hilbert space.^{67,76,77} [We note in the limit of a two-dimensional Hilbert space, the complete and reduced unfiltered schemes are equivalent.] One can develop additional evolution schemes where all of the above are combined, and these will be considered as part of future studies.

Finally, it is perceivable that certain sequences of intermediate, noncommuting measurements can maximize $\{\sum_m \langle A_m | \rho_N | A_m \rangle\}$ and drive $|D\rangle$ to $\{|A_m\rangle\}$ more efficiently than others.⁶⁰ For example, one might treat eqs 4, 7, and 9 as multidimensional optimization problems with respect to the unknowns θ_I , $\langle M_{j_I}^I | M_{j_{I-1}}^{I-1} \rangle$, and $\langle M_{j_I}^I | M_{j_{I-1}}^{I-1} \rangle$. Additionally, the measurement operators can be optimized, which will also affect the filtered measurement process. The goal of optimal control experiments,^{59,67,68} which make use of measurement-driven evolution, is to find the set of parameters which allow $\{\hat{\mathcal{N}}_I\}$ to maximally drive the $|D\rangle$ state to the $\{|A_m\rangle\}$ states for a given number of measurements. In this paper, we view the enzyme as generating a control field, and we examine how the parameters already “chosen” by SLO-1 affect the proton transfer reaction, utilizing the measurement schemes described above. An exploration of the field parameters is explored in section III.D by changing the measurement sequence.

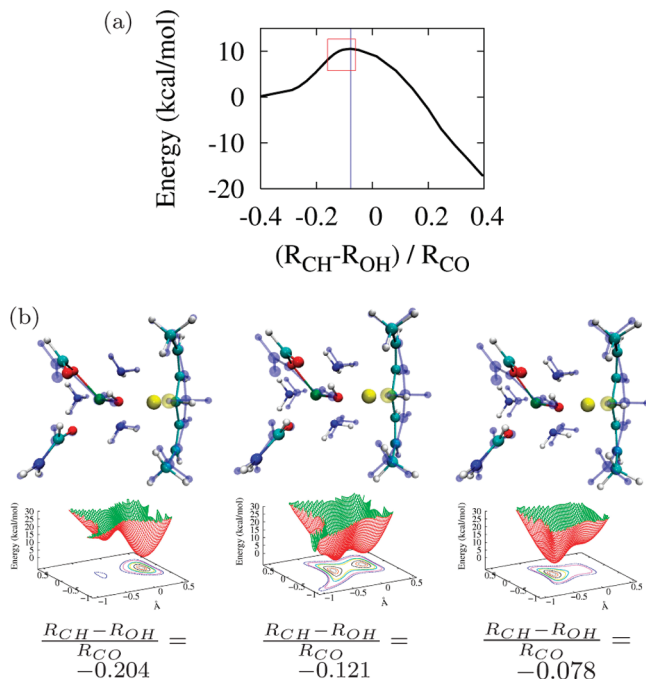


Figure 3. (a) The minimum energy reaction profile for the rate determining step [Figure 1a] in SLO-1. The critical tunneling region is highlighted with a box, and the classical transition state is shown using a vertical line. The horizontal axis is a reduced coordinate that only includes the distances between the donor carbon, the tunneling proton, and acceptor oxygen. However, it is important to note that, *for every point along this reaction coordinate, the entire active site geometry changes*. That the quantity $(R_{\text{CH}} - R_{\text{OH}})/R_{\text{CO}}$ only indicates a measure of this effect is shown in the upper portions of b, which depict the entire active site model at different points along the reaction coordinate. The transferring hydrogen is enlarged and highlighted in yellow, and the blue transparent system represents the initial, reactant geometry. Finally, the bottom panels of b depict two-dimensional cuts of the three-dimensional, hydrogen nuclear potential surface [$V_I^{\text{DFT}}(R_{\text{H}}; \{\mathbf{R}_{\text{as}}\})$ of eq 11] at a reactant, tunneling region, and classical transition state active site geometry, respectively. [The exact placement on the reaction coordinate is indicated by the captions.] The x and y coordinates correspond to the hydrogen nuclear position at each active site geometry.

III. Measurement-Induced Control as Applicable to Hydrogen Nuclear Tunneling in SLO-1

A. Definition of $\{\hat{\mathcal{M}}_I\}$, $|D\rangle$, and $\{|A_m\rangle\}$. In this section, we apply the methods described in section II to the hydrogen transfer in SLO-1. The enzyme active site is treated here as a measurement device. To achieve this, we utilize the potential energy surfaces computed in ref 26, where, as discussed earlier, we studied active site models of SLO-1 using quantum wavepacket dynamical treatment of the transferring H/D nucleus along with treatment of electrons at the level of DFT, benchmarked through MP2 calculations. To maintain correspondence between the active site geometries and the measurement operator, we first define our intermediate measurement operators, $\{\hat{\mathcal{M}}_I\}$, as the hydrogen nuclear Hamiltonians generated by each active site geometry along the reaction path depicted in Figure 3a. It is important

to note that, while Figure 3a displays a simplified reaction coordinate, in fact the entire active site geometry [see Figure 3b] changes at each point²⁶ along the axis. Figure 3b displays a set of selected active site geometries encountered as one moves along the direction indicated by the horizontal axis in Figure 3a. The measurement operators are the effective Hamiltonian operators that describe the dynamics of the tunneling hydrogen or deuterium atom, under the influence of the active site.

$$\hat{\mathcal{M}}_I \equiv \hat{H}_I = \sum_j \epsilon_j^I |\epsilon_j^I\rangle \langle \epsilon_j^I| = \sum_j \epsilon_j^I \hat{P}_I^j \quad (10)$$

Here, ϵ_j^I and $|\epsilon_j^I\rangle$ are the eigenenergies and eigenvectors of the Hamiltonian \hat{H}_I :

$$\hat{\mathcal{M}}_I \equiv \hat{H}_I = -\frac{\hbar^2}{2m_{\text{H}}} \nabla_{R_{\text{H}}}^2 + V_I^{\text{DFT}}(R_{\text{H}}; \{\mathbf{R}_{\text{as}}\}) \quad (11)$$

where, as noted earlier, R_{H} represents the position of the proton or deuteron and $V_I^{\text{DFT}}(R_{\text{H}}; \{\mathbf{R}_{\text{as}}\})$ is the density functional potential at R_{H} , that also depends on the active site geometry, $\{\mathbf{R}_{\text{as}}\}$. [The eigenfunctions, eigenenergies, and potential surfaces of each operator were calculated in ref 26 using the Arnoldi diagonalization scheme.^{78,79}] Figure 3b depicts the change in potential, $V_I^{\text{DFT}}(R_{\text{H}}; \{\mathbf{R}_{\text{as}}\})$, in the critical portion of the measurement (Hamiltonian) operators along the direction of the horizontal axis in Figure 3a. Thus, each measurement operator depends on the corresponding active site geometry and electronic structure via the potential energy term in the Hamiltonian, \hat{H}_I . [This is similar to the magnetic field in the Stern-Gerlach experiments.] We envision that the state of the proton at each point along the reaction path is influenced by the measurement apparatus [active site geometry].

In the following sections, we examine how these measurement operators may drive the proton from the donor state, identified as $|D\rangle$, to the subspace of acceptor states, $\{|A_m\rangle\}$. To accomplish this, we only consider the tunneling region which was determined in ref 26 to be $-0.2 \leq (R_{\text{CH}} - R_{\text{OH}})/R_{\text{CO}} \leq -0.06$ and is shown in the boxed region in Figure 3a. The states $|D\rangle$ and $\{|A_m\rangle\}$ were chosen on the basis of how well the proton and deuteron eigenstates are localized in their respective donor carbon and acceptor oxygen basins,²⁶ and on the donor–acceptor orthogonality condition. Some properties of the chosen states are described in Table 1. [Although only the ground acceptor state is featured, the first five states have similar characteristics to those displayed in the table, e.g., $\cos^{-1}(\langle D|A_m\rangle) = 90.0^\circ$ for $m = 1-5$ for both hydrogen and deuterium.]

B. Filtered Measurements by the SLO-1 Active Site.

1. Single Measurement. Here, using eq 1, we examine the effect of a single measurement acting on the donor state, to identify critical regions along the reaction coordinate based on the effectiveness of the active site in driving population to the acceptor states. The index I in eq 1 now refers to a point along the reaction coordinate shown in Figure 3a. The results are shown in the middle panels of Figure 4 for (i) one acceptor state and two-dimensional measurements [$N_{\text{A}} = 1$ and $N_{\text{DM}} = 2$ in eq 1] and (ii) a subspace of acceptor

Table 1. Summary of the Donor, $|D\rangle$, and Acceptor, $|A_m\rangle$, Subspaces Utilized in the Measurement Process^a

	$(R_{CH} - R_{OH})/R_{CO}$	$R_{CH}/(\text{\AA})^b$	$R_{OH}/(\text{\AA})^c$	$\sigma_{DA}(\text{\AA})^d$	θ_{TS}^e	θ_A^f
$ D\rangle$	-0.201	1.11	1.71	0.0738 (0.0612)	89.8 (90.0)	90.0 (90.0)
$ TS\rangle$	-0.0778	1.68	0.98	0.0822 (0.0652)	0	7.0 (8.1)
$ A_1\rangle$	-0.0586	1.69	0.98	0.0765 (0.0643)	7.0 (8.1)	0

^a The values within parentheses are for deuterium. ^b Distance between the $|D\rangle$ (donor), $|TS\rangle$ (classical transition state), and $|A_1\rangle$ (ground acceptor state) centroids and the donor carbon. ^c Distance between the $|D\rangle$, $|TS\rangle$, and $|A_1\rangle$ centroids and the acceptor oxygen. ^d $\langle (R_H^D - \langle R_H^D \rangle)^2 \rangle^{1/2}$, where R_H^D is the proton (deuteron is R_D^D) coordinate parallel to the donor-acceptor axis. ^e Angle formed with the classical transition state vector, $|TS\rangle$, in degrees. [$\equiv \cos^{-1}(\langle X|TS \rangle)$], where $|X\rangle$ is $|D\rangle$, $|TS\rangle$ or $|A_1\rangle$. ^f Angle formed with the acceptor ground state vector, $|A_1\rangle$, in degrees. [$\equiv \cos^{-1}(\langle X|A_1 \rangle)$].

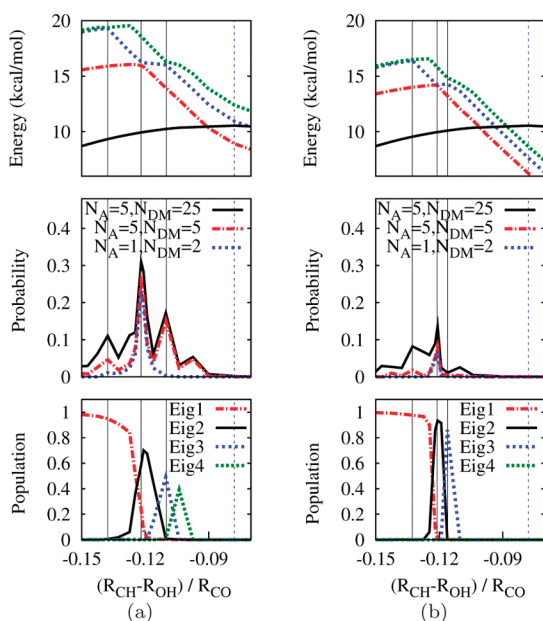


Figure 4. (Top) The classical reaction profile [black curve] and the first three (a) hydrogen and (b) deuterium eigenenergies, along the reaction coordinate. These energies drop below the reaction path surface since the eigenstates close to the top of the barrier are localized on the product side and hydrogen tunneling shifts the “transition state” toward the reactant. The middle panels depict the probability of driving the donor state to the acceptor subspace after one measurement for (a) proton and (b) deuteron taken at the corresponding point on the reaction coordinate. The dimensionalities of the measurements are indicated by N_A and N_{DM} [see eq 3], and the vertical axes’ scales are maintained to exemplify the effect of measurement-driven transfer probability for the proton and deuteron. The bottom panels are the instantaneous wavepacket components along the time-dependent eigenstates for the (a) proton and (b) deuteron. Nuclear excited state contributions are critical in both cases. The curve crossings between eigenstates 2 and 3 and the avoided crossings between eigenstates 1 and 2, and 2 and 3 (left to right) are indicated by the gray, solid, and vertical lines. All panels have the same horizontal axis. The position of the classical transition state is also shown using the vertical, dotted, blue line.

states [$N_A = 5$] and multidimensional measurement operators [$N_{DM} = 5$ and 25]. The horizontal axis in Figure 4 is the

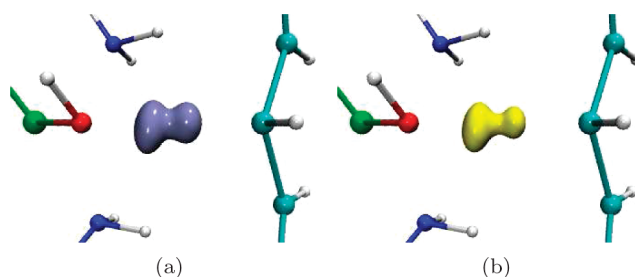


Figure 5. Ground eigenstates for the (a) proton and (b) deuteron at the maximum zero-point corrected energy point, $(R_{CH} - R_{OH})/R_{CO} = -0.121$. The spread along the donor-acceptor direction for the states displayed is $\langle (R_H^D - \langle R_H^D \rangle)^2 \rangle^{1/2} = 0.240 \text{ \AA}$ for hydrogen and equal to 0.173 \AA for deuterium; i.e., the hydrogen nuclear state is only slightly more delocalized. Additionally, the included angles of these states with the donor ($|D\rangle$) and acceptor ($|A_1\rangle$) states in Table 1 are $\langle H_{-0.121}|D\rangle = \cos(68.1^\circ)$, $\langle D_{-0.121}|D\rangle = \cos(78.4^\circ)$ and $\langle H_{-0.121}|A_1\rangle = \cos(39.5^\circ)$, $\langle D_{-0.121}|A_1\rangle = \cos(28.5^\circ)$. These data represent the fact that both states (in parts a and b) are relatively closer to the acceptor state than to the donor state, which is also clear from the larger left lobe in both figures.

reduced reaction coordinate of Figure 3, and each point corresponds to a measurement operator. The results for hydrogen are presented in Figure 4a, while those for deuterium are presented in Figure 4b.

The top panels in Figure 4 are the eigenstate energy profiles, i.e., ϵ_j^I from eq 10, as a function of I , and the bottom panels are the dynamical eigenstate populations as calculated from the quantum wavepacket dynamical studies in ref 26. From Figure 4, we note that first, quantum mechanical transfer of population occurs over a range. This range is N_{DM} dependent and is wider for the proton than for the deuteron. [This aspect is also noted for the sequential measurements discussed in section III.B.3 and is further discussed at the end of section III.C.] We also note from the middle panels that the probability for proton transfer into an acceptor state, as a result of the single measurement, is always greater than for deuteron transfer. Furthermore, for each dimensionality studied, a single measurement at $(R_{CH} - R_{OH})/R_{CO} \approx -0.121$ has maximal transition promoting effect. The origin of the measurement operator situated at $(R_{CH} - R_{OH})/R_{CO} \approx -0.121$ coincides with the appearance of an avoided crossing between the ground and first excited hydrogen nuclear eigenfunction as noted in the top panels in Figure 4a and b. This also coincides with the point on the bottom panel in Figure 4a and b where a transfer of population occurs between the ground hydrogen nuclear state to the first excited hydrogen nuclear state. Therefore, the measurement at $(R_{CH} - R_{OH})/R_{CO} \approx -0.121$ may be interpreted as being germane to both proton as well as deuteron transfer. However, this is to be expected on the basis of the delocalized nature of the ground hydrogen nuclear state at $(R_{CH} - R_{OH})/R_{CO} \approx -0.121$ shown in Figure 5. Note further that the point $(R_{CH} - R_{OH})/R_{CO} \approx -0.121$ is not the classical transition state but is situated on the reactant side as seen in Figure 3a. Thus, the measurement at $(R_{CH} - R_{OH})/R_{CO} \approx -0.121$ leads to hydrogen/deuteron tunneling, where hydrogen tunneling is clearly more probable.

Additionally, it is apparent from Figure 4a and b that all measurement operators that have an effect on population transfer from a donor state to an acceptor state are supported by curve crossings in the nuclear eigenstate manifold [top panels of Figure 4]. It is also clear that the curve crossings do not occur at the same points along the proton and deuteron reaction surfaces, which distinguishes the process of hydrogen tunneling from deuterium tunneling from a single measurement perspective. In fact, even the avoided crossing between the ground and first excited state and the associated maximum point in the middle panels of Figure 4 discussed above are not at the same point, although they are very close. This implies that different measurement operators may play a role in promoting H or D, but it appears that the geometries close to -0.121 are of fundamental importance for both transfer processes. This aspect will be probed to a greater extent in section III.D when we study measurement-assisted control of the H/D transfer process, with a greater focus on this region of the reaction coordinate.

The above analysis also shows that curve crossings not only allow nonadiabatic population transfers, as shown in the bottom panels in Figure 4, but also facilitate transfer of population from donor to acceptor states. This is consistent with the relatively large angles between the hydrogen-nuclear eigenstates in this region and the acceptor states, as might be clear upon inspection of Figure 5. Hence, the idea that the tunneling process may be measurement-driven, where the measurement is constructed by the active site dynamics and its interaction with the tunneling nucleus, is an appealing consequence of this analysis. It is important to underline the fact that the analysis depicted through the middle panel in Figure 4 only includes the computation of probabilities as dictated by eq 1, for a chosen set of $|D\rangle$ and $\{|A_m\rangle\}$ states and a single measurement operator [$N_I = 1$ in eq 3].

2. Commutators as a Metric to Probe Sensitive Regions on the Reaction Surface. Once a measurement has been made by operator $\hat{\mathcal{M}}_I$, the incremental disturbance due to measurement $\hat{\mathcal{M}}_{I+1}$ is zero if the measurement operators $\hat{\mathcal{M}}_I$ and $\hat{\mathcal{M}}_{I+1}$ commute, since this implies that the operators have simultaneous eigenstates. Therefore, we can quantify the perturbation to the system caused by subsequent measurements by computing the magnitude of $[\hat{\mathcal{M}}_{I+1}, \hat{\mathcal{M}}_I]_\beta \equiv [H_{I+1}, H_I]_\beta \equiv [H_2, H_1]_\beta$, where the subscript β is the inverse temperature and is included to filter out unphysical (i.e., high energy) eigenstates through Boltzmann weighting. In other words, we compute

$$\begin{aligned} \|[\hat{\mathcal{M}}_{I+1}, \hat{\mathcal{M}}_I]_\beta\|_F &\equiv \| [H_{I+1}, H_I]_\beta \|_F \approx \\ &\left\| \left[\sum_k \exp[-\beta \epsilon_k^{I+1}] \epsilon_k^{I+1} P_{I+1}^k, \sum_j \exp[-\beta \epsilon_j^I] \epsilon_j^I P_I^j \right] \right\|_F \end{aligned} \quad (12)$$

where “ $\|\dots\|_F$ ” indicates the Frobenius norm⁷⁹ of the commutator.

The evolution of eq 12 for both hydrogen and deuterium at several temperatures is provided in Figure 6. We note from this figure that, in the vicinity of $(R_{CH} - R_{OH})/R_{CO} \approx -0.121$, there is a large spike for the hydrogen and smaller spike for the deuterium commutators at low temperatures. This large

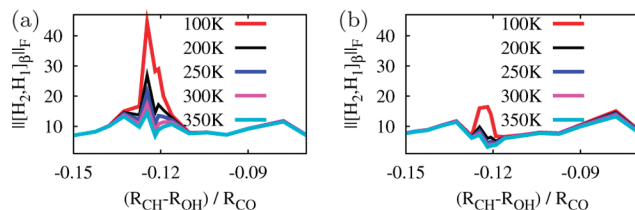


Figure 6. The Frobenius norm of the thermally reduced Boltzmannized subspace commutator [eq 12] at different temperatures depicted for (a) hydrogen and (b) deuterium.

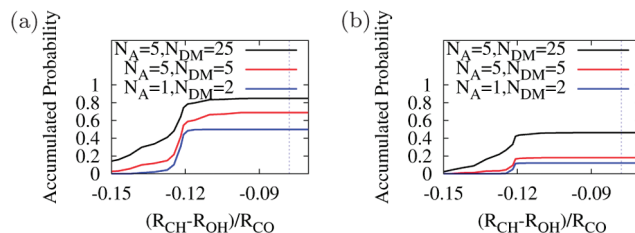


Figure 7. The accumulated probability of driving the donor state to the acceptor subspace after N_I measurements for the (a) proton and (b) deuteron. The dimensionality of the measuring process is indicated by N_A and N_{DM} [see eq 3]. The classical transition state is the vertical, dotted blue line.

change is an indication of the importance of this region, as already established in the previous sections. However, this spike becomes less significant as more excited states are included [i.e., as temperature increases]. As outlined above, eq 12 is a Boltzmannized self-similarity metric of subsequent measurement operators. Clearly, Figure 6 indicates that the self-similarity of subsequent measurement operators in the vicinity of $(R_{CH} - R_{OH})/R_{CO} \approx -0.121$ is greater for D than for H at all temperatures, and quite pronounced at lower temperatures, which in turn leads to the result that the ground states of D, along $(R_{CH} - R_{OH})/R_{CO}$, are more self-similar than H. This has an important effect on the transfer process.

3. Sequential Measurements. Next, we consider a sequence of filtered measurements as described by eq 3. Here, the probability of projecting the initial state onto the $\{|A_m\rangle\}$ subspace is accumulated over a set of measurements along the reaction coordinate. This calculation examines the cumulative effectiveness of the concatenated sequence of measurements [i.e., the active site geometric evolution] in promoting the transfer of the hydrogen nucleus. Each intermediate measurement is followed by an interrogation of the donor/acceptor space as described in section II.A. We have utilized $N_I = 29$ in eq 3 [that is, 29 measurements in the tunneling region highlighted within the box in Figure 3a] for the results displayed in Figure 7. Again, we notice that the tunneling from donor to acceptor takes place over an N_{DM} -dependent range of active site geometries similar to those already noted in Figure 4. In addition, the proton transfer probability is always greater than the deuteron probability. The evolution of transfer probabilities follows a sigmoid-like behavior, where the inflection point occurs near $(R_{CH} - R_{OH})/R_{CO} \approx -0.121$, which corresponds to the point in Figure 4 displaying maximal transfer probability from donor to acceptor. Furthermore, we note that H-transfer appears to occur over a wider range in Figure 7, as is

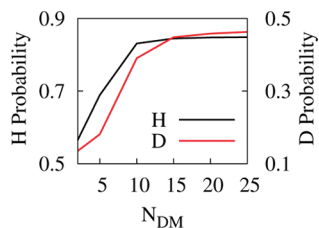


Figure 8. The accumulated probability in the vicinity of the classical transition state as a function of N_{DM} for protium and deuterium. Note that the hydrogen curve plateaus at $N_{DM} \approx 10$ –15, whereas the deuterium still has not fully plateaued at $N_{DM} = 25$. [Note that the y-axis ranges are the same for protium and deuterium.]

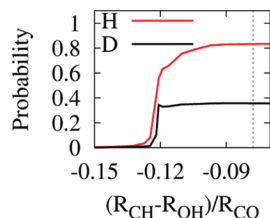


Figure 9. Probability of driving the donor [$|D\rangle$] population to the acceptor [$|A_m\rangle$] as a function of the reaction coordinate, calculated from eq 7. Here, $N_{DM} = 25$ and $N_A = 5$. The blue, dotted, vertical line is the classical transition state.

expected on the basis of the wider range of single measurements that contribute to donor→acceptor probability transfer in Figure 4.

Upon inspection of the converged transfer probabilities in the vicinity of the classical transition state [see Figure 7], we note that deuterium transfer is more sensitive to N_{DM} than protium transfer. Since N_{DM} represents the size of the measurement operator subspace, this implies that excited states participate to a greater extent in deuterium transfer than protium transfer. This property is confirmed through Figure 8, which displays a slower convergence of the transfer probability as a function of N_{DM} for deuterium. A similar result was obtained in ref 26 using quantum wavepacket dynamics.

C. Unfiltered Measurements by the SLO-1 Active Site. *1. Complete Space.* We now consider an unfiltered measurement process over the expanded measurement space ($N_{DM} = 25$ in section II.B.1), since the expanded space is required to fully describe the transfer in this scheme. The probability of reaching the acceptor space along the reaction coordinate is shown in Figure 9. Although this process favors proton over deuteron transfer and the proton transfer width is greater, a comparison of Figure 9 to Figure 7 shows that the proton and deuteron transfer range is tighter here. In other words, the reaction coordinate range with a growing population in the acceptor states is narrower here since the process depicted in Figure 9 allows for probability to flow freely between the donor and acceptor spaces, whereas the procedure depicted in Figure 7 prevents backflow. Figure 9 shows that the $\{|A_m\rangle\}$ population grows rapidly near $(R_{CH} - R_{OH})/R_{CO} \approx -0.121$, which coincides with the appearance of an avoided crossing between the ground and first excited proton eigenfunctions as discussed in section III.B.1. Again, the

proton and deuteron transfer probability become significant before the classical transition state is reached.

2. Reduced Space. Before analyzing the reduced space measurements, we must decide on the $\{P^k\}$ subspace. Henceforth, the explicit dependence of k on I is dropped for simplicity [see eq 9 in section II.B.2]. To gain an understanding of the role of this subspace, we consider $\{P^k\}$ with a span of one [i.e., each $\{P^k\}$ consists of one vector]. We also want to determine the conditions under which this subspace is the dominant path for $|D\rangle \rightarrow \{|A_m\rangle\}$ transfer. In other words, we wish to choose our subspace to maximize transfer through the path $|\langle A_m | \prod_I P_i^k | D \rangle|^2$, where $P_i^k = |M_i^k\rangle\langle M_i^k|$. Equivalently, we optimize $\prod_I \cos \theta_I$, where $\cos \theta_I = \langle M_i^{I+1} | M_i^I \rangle$. We place an additional constraint on this optimization problem by requiring that the angles, θ_I , sum to $\phi = \pi/2$. This equality holds if the $\{|D\rangle; |A_m\rangle\}$ space spans the $\{P^k\}$ space. Therefore, we solve

$$\frac{\partial}{\partial \theta_J} \left\{ \prod_I \cos \theta_I - \lambda \left(\sum_I \theta_I - \phi \right) \right\} = 0 \quad (13)$$

where λ is a Lagrange multiplier equivalent to $-\sin \theta_J \prod_{I \neq J} \cos \theta_I$. This expression then leads to

$$\frac{\tan \theta_J}{\tan \theta_K} = 1 \quad (14)$$

for all J and K or

$$\theta_J = \theta_K + n\pi \quad (15)$$

where n is an integer. Thus, if the span of the subspace $\{P^k\}$ is unity, then it is obviously true that all angles, θ_I , must be equal. But if the subspace size is greater than one, the constraint above is modified in that there must exist at least one path $\{\theta_I^{K(I)}\}_{\forall I}$ such that $\sum_I \theta_I^{K(I)} \geq \pi/2$. The equal angle relation may not hold then between eigenstates of consecutive measurement operators. The equal angle result is identical to that derived by Pechen and co-workers in ref 67.

In our case, the ground state projectors, $\{P\}$, approximately satisfy the equal-angle relation almost everywhere along the reaction profile except in the vicinity of $(R_{CH} - R_{OH})/R_{CO} \approx -0.121$. This central region is complicated by the presence of the avoided crossing and is characterized by a rapid change in wavepacket morphology. Hence, we infer that, while the evolution obeys a two-dimensional Hilbert-space paradigm away from the high-interaction region, the existence of a large number of avoided crossings in the vicinity of $(R_{CH} - R_{OH})/R_{CO} \approx -0.121$ couples the multiple proton vibrational states. This result is consistent with previous studies and strongly suggests the nonadiabatic nature of hydrogen transfer in the vicinity of $(R_{CH} - R_{OH})/R_{CO} \approx -0.121$.

Working from this proposition, matrix elements of ρ_I in eq 9 may be written as

$$\rho_{i,j}^I \equiv \langle M_i^I | \rho_I | M_j^I \rangle = \prod_{k \in k} |1 - \{\delta_{i,k'} + \delta_{j,k'}\}| \times \sum_{l,n}^{N_{DM}} \rho_{l,n}^{I-1} \cos \theta_{M_i^I, M_l^{I-1}} \cos \theta_{M_j^I, M_n^{I-1}} \quad (16)$$

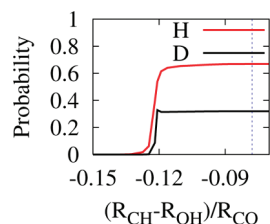


Figure 10. Probability of driving the donor $[D]$ population to the acceptor $[A_m]$ as a function of the reaction coordinate, calculated from eq 16. Here, $N_{DM} = 25$ and $N_A = 5$. The blue, dotted, vertical line is the classical transition state.

Therefore, the density matrix has the property that, after its measurement, only the ground state is diagonal in the \hat{M}_I representation. This is an important distinction between the measurement paradigm chosen in this section as opposed to that in the previous sections. That is, in this case the measurement does not affect the $[I - \sum_{\{k\}} P_k^\dagger] \rho_I [I - \sum_{\{k\}} P_k]$ block of the density matrix, since $[I - \sum_{\{k\}} P_k^\dagger]$ is a reduced-dimensional identity operator and the transfer occurs only due to the elimination of the $P_k^\dagger \rho_I [I - P_k^\dagger]$ coherences. Therefore, the transfer probabilities are determined by the morphology of the measurement operator eigenstates in the $\{P^k\}$ subspace.

The accumulated transfer probabilities, as seen in Figure 10, have very tight, classical-like proton transfer widths. Furthermore, the transfer probability becomes significant in the vicinity of $(R_{CH} - R_{OH})/R_{CO} \approx -0.121$, which is characterized by a change in morphology of the ground state. Thus, it appears that one set of deviations from classical-like transfers arises when multiple states are measured; i.e., the nonlocality of the transfer paths in the energy representation results in nonlocality of the hydrogen nuclear transfer over the reaction coordinate. [Another reason for deviations from classical behavior is already noted to be due to a shift in the critical transfer region from the classical transition state to $(R_{CH} - R_{OH})/R_{CO} \approx -0.121$, and both of these deviations are consistent with those already seen in the wavepacket dynamics studies in ref 26.] We further find that the final transfer probability is smaller in Figure 10 compared to Figure 9, since an additional 3% of the probability lies beyond the first 25 proton eigenstates at the end of the reaction coordinate and 5% lies beyond the first 25 deuterium eigenstates.

Finally, a few comments are warranted about the results given in the previous sections. First, several of the qualitative features found in the wavepacket dynamics studies in ref 26, such as (a) the shift in the “transition state” toward the reactant as a result of nuclear quantization, (b) greater participation of excited states in the case of deuterium, and (c) the presence of critical points along the reaction coordinate that facilitate hydrogen and deuterium transfer and coincide with surface crossings, are also recovered using the measurement perspective. But, the transfer probabilities obtained in the sections above indicate that measurement alone is not the only factor to consider when looking at the proton transfer in SLO-1. For example, the unitary evolution of the wavepacket on changing potential energy surfaces, which was utilized to reproduce the experimental KIE,²⁶ is

not utilized in the process depicted here. This suggests that the hydrogen transfer process in SLO-1 may be interpreted as a combination of measurement-driven and unitary evolution. Such a combination has been found to accelerate processes in several other studies.^{65,67}

Another important factor that should be discussed relates to the role of donor–acceptor distance in tunneling. This aspect has received considerable attention in the literature.^{6,9,10,18–21,25,32,80,81} In our quantum dynamics study of ref 26, we found that, as the donor–acceptor distance increased, the H-transfer probability was much greater than the D-transfer probability [see the dotted line in Figure 13 of ref 26]. This result is to be expected, since for a given potential surface, a particle with a larger de Broglie wavelength tunnels through larger distances. This implies that H-tunneling will occur over a larger donor–acceptor distance, and this result is consistent with what we see in ref 26 and also with that obtained from other groups.^{18,19,21,25} One can make a similar qualitative deduction on the basis of the broader nature of hydrogen transfer curves in Figures 4 [central panel], 7, 9, and 10, which indicate that hydrogen transfer does occur over a broader donor–acceptor distance. These results are, of course, computed without quantum dynamical evolution, whereas those in ref 26 include quantum dynamical evolution.

D. Measurement Assisted Control. In this section, we describe a numerical experiment we performed that illustrates the control the active site measurement device may exert over the tunneling hydrogen or deuterium nucleus. In this experiment, we explored how a small perturbation to the sequence of measurements [i.e., active site dynamics] might affect the transfer probabilities. *In vivo*, mutations to the amino acid sequence might be responsible for a similar perturbation to the overall dynamics of the active site. [Certain mutations have been shown to noticeably affect transfer properties in SLO-1.^{80,82,83}] Our perturbation consists of permuting the order of active site measurements in small regions along the reaction coordinate. In particular, we chose sets of six consecutive measurements, each set from a different region of the reaction coordinate, and permuted the order in each set, one region at a time. For example, while retaining the original sequence in other areas of the reaction coordinate, we permuted all three measurements [or active site geometries] in the range $-0.125 \geq (R_{CH} - R_{OH})/R_{CO} \geq -0.121$ and combined them with permutations of all three geometries in the subsequent range of $-0.119 \geq (R_{CH} - R_{OH})/R_{CO} \geq -0.110$. From the discussion in earlier sections, the transfer probabilities associated with these regions may be expected to be significant. We then used the new order to recalculate eq 7 as an illustration, since this measurement scheme is order sensitive and it describes the entire transfer event with the first 25 proton/deuteron eigenstates. Permuting the measurement operators [and the corresponding active site geometries] is expected to provide an alternative approach to probe the role of active site reorganization on the hydrogen transfer process. For instance, in regions of the reaction coordinate where the active site atoms actively facilitate the H-transfer, one would expect a larger effect from permutation. In an enzyme, suitable active site mutations can give

Table 2. Magnitude and Effect of Perturbation to the Active Site Dynamics Sequence

$(R_{\text{CH}} - R_{\text{OH}})/R_{\text{CO}}$ range	$\langle R_{\text{DA}} \rangle^a$	ΔR_{DA}^b	ΔR_{as}^c	$\Delta \theta^d$	$\rho_{N_i}^e$
−0.197 to −0.180	2.78	3.88×10^{-3}	8.54×10^{-5}	2.3 (2.6)	82.4 (35.4)
−0.152 to −0.127	2.69	2.51×10^{-3}	2.43×10^{-4}	5.4 (4.9)	79.3 (35.9)
−0.125 to −0.110	2.67	1.10×10^{-3}	1.57×10^{-4}	12.2 (32.0)	69.1 (39.5)
−0.110 to −0.0671	2.66	6.82×10^{-4}	5.32×10^{-4}	4.8 (5.1)	79.2 (35.2)

^a The average donor–acceptor distance in Å computed using only geometries in the given reaction coordinate range. ^b Change in the donor–acceptor distance sequence between the perturbed and unperturbed measurement sets: $1/6(\sum(R_{\text{DA}} - R_{\text{DA}}^{\text{pert}})^2)^{1/2}$, in Å. The factor of 6 occurs since each range contains six geometries, all of which are involved in the permutation. ^c Change in the active site geometry sequence between the perturbed and unperturbed measurement sets. This is computed using the active site distance matrices. ^d Angle between the ground proton (deuteron) eigenstate sequence in degrees. ^e Final transfer probability for the proton (deuteron) calculated using eq 7. The original transfer probability is 83.4 (35.6).

rise to a similar effect through structural [electronic and steric] as well as dynamical [fluctuations in active site structure] influence.

We found the final transfer probabilities change most significantly when measurement operators were reordered in the critical range of $-0.124 \geq (R_{\text{CH}} - R_{\text{OH}})/R_{\text{CO}} \geq -0.110$ according to

$$\{\{M1, M2, M3\}; \{M4, M5, M6\}\} \rightarrow \{\{M1, M3, M2\}; \{M5, M6, M4\}\} \quad (17)$$

where the left-hand side represents the original sequence of measurement operators and active site geometry evolution. The fact that this perturbation has an important impact can also be gauged from the fact that *M3* above was at $(R_{\text{CH}} - R_{\text{OH}})/R_{\text{CO}} = -0.121$. Thus, the perturbation above has the effect of modifying the active site dynamics in the vicinity of $(R_{\text{CH}} - R_{\text{OH}})/R_{\text{CO}} = -0.121$ according to $\{M2, M3, M4\} \rightarrow \{M3, M2, \dots, \dots, M4\}$. That is, the ordering of active site dynamics in the vicinity of this critical point is completely changed.

The extent of the perturbation in eq 17 in four regions spanning the reaction coordinate is displayed in Table 2, where the critical region is bold. The perturbations give rise to a combined electronic and structural effect and are quantified as follows: Since altering the dynamical sequence changes the time evolution of donor–acceptor distances, we present a measure of this change, ΔR_{DA} , in the third column. The average donor–acceptor distance inside each perturbed reaction coordinate range is presented in the second column. We also provide a measure of the perturbation to the sequence of active site geometries, ΔR_{as} , in column four and the perturbation to the ground eigenstates, $\Delta \theta$, in column five. The combined [structural and electronic] effect of these perturbations on the final population transfer is presented under the sixth column, labeled ρ_{N_i} .

The following aspects become apparent upon inspection of Table 2. First, we notice that the perturbation in the critical tunneling range (third row) has the largest effect on the transfer probabilities. Changes to this region decrease the proton transfer probability by 14% and increase the deuteron transfer probability by 4%. The original transfer probabilities are 83% for the proton and 36% for the deuteron. Also, the proton transfer probability is more sensitive to the measurement order than the deuteron, and no perturbation that we explored increased the proton transfer probability, although increases in the deuteron transfer probability did occur.

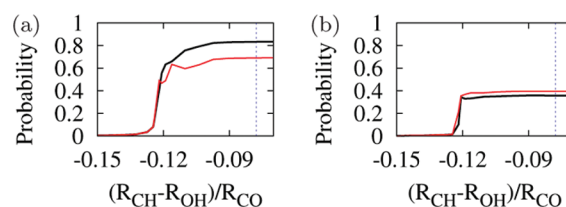


Figure 11. Probability of driving the donor [*ID*] population to the acceptor [*|A_m*] as a function of the reaction coordinate, calculated from eq 7 for (a) the proton and (b) the deuteron. Here, $N_{\text{DM}} = 25$ and $N_A = 5$. The black curves represent the unperturbed transfer, whereas the red curves are the transfer when the perturbation described in the text is applied to the critical $-0.125 \geq (R_{\text{CH}} - R_{\text{OH}})/R_{\text{CO}} \geq -0.110$ region. The blue, dotted, vertical line is the classical transition state.

The values in Table 2 again indicate the importance of the critical -0.125 to -0.110 region, and in particular the importance of the active site sequence. Although the size of the perturbation to the active site structure, as measured by ΔR_{DA} and ΔR_{as} , may be relatively larger in other areas, this does not translate into a large effect on the transfer probability. However, the localization of the perturbation to the critical region results in a large difference. The reason for this is seen by examining $\Delta \theta$, which indicates how the potential surfaces affect the hydrogen nuclear eigenstates near the zero-point region. Clearly, the sensitivity of the proton and deuteron eigenstate shape to the changes in the underlying potential energy surfaces, which are double-well in this region [see Figure 3b], is responsible for the large effect on the probability transfer.

The transfer probability curves for the perturbation discussed in this section applied to the critical region are depicted in Figure 11. These figures indicate that the permutation results in a region of net backflow for proton transfer as seen from the reduction in transfer probability of the red curve in Figure 11a to the right side of -0.12 . Such backflow can be understood from a transition state theory perspective. If we imagine a dividing surface between $|D\rangle$ and $|A_m\rangle$, measurements that result in a higher transfer probability are indicative of more forward than backward crossings [i.e., a higher ratio of productive Hilbert space paths in eq 7 to unproductive paths], whereas measurements that result in a lower transfer probability are indicative of the opposite. Thus, these permutations can be seen to move the

dividing surface, which results in a changing ratio of forward and backward crossings or productive and unproductive paths.

IV. Conclusions

In a previous publication,²⁶ we examined the properties of the hydrogen transfer reaction in soybean-lipoxygenase-1 (SLO-1) by computing three-dimensional hydrogen nuclear potential energy surfaces at points along the reaction coordinate using *ab initio* electronic structure methods. From these surfaces, we were able to generate proton and deuteron eigenstates. On the basis of these calculations, we explore a rather fascinating concept in this publication, where the active site motion in SLO-1 projects the hydrogen nuclear state onto intermediate energy eigenstates, which depend on a time-dependent potential. This process may cause measurement-driven evolution of the quantized hydrogen and deuterium atoms. Thus, in this publication, we viewed the SLO-1 active site as a “measurement device” that alters the quantum state of the hydrogen nuclear wavefunction.

Three possible mechanisms for this process were proposed and explored. From these different schemes, we were able to reproduce many of the *qualitative* features found using quantum wavepacket dynamical studies.²⁶ For instance, we note that the proton and deuteron begin to have significant population transfer near $(R_{\text{CH}} - R_{\text{OH}})/R_{\text{CO}} \approx -0.121$, which occurs *before the classical transition state*. Our results also indicate that excited states play a more important role in deuteron transfer than in proton transfer, since the deuteron transfer probability has a stronger dependence on the measurement operator dimensionality.

The measurement theory paradigm also provides us with new insights. For example, we note in section III.B.1 that the eigenstates located at curve crossings maximize transfer from donor to acceptor subspaces, whereas the avoided crossings in the unitary evolution picture allow for transfer between eigenstates. This result is related to the work of Modi and Shaji,⁸⁴ where they show that an experimentally observed⁸⁵ anti-Zeno effect occurs only due to the existence of an intermediate state between the ground/bound (donor) and vacuum/decay (acceptor) states. Likewise, at our avoided crossings, there are two, nearly degenerate states which mediate between the donor and acceptor states. Furthermore, we explored the properties of a novel metric for the self-similarity between the consecutive, active-site geometry-dependent Hamiltonians. This measure grows more in the critical transfer region for a proton than a deuteron. This behavior is indicative of an active site sequence that transfers a proton more efficiently than a deuteron.

Finally, we note that perturbations to the order of active site dynamics can have an important effect on the transfer probabilities. In conclusion, the measurement paradigm captures some of the qualitative ideas seen earlier from full quantum wavepacket dynamical studies²⁶ but does not quantitatively describe the effect of the SLO-1 enzyme active site during the hydrogen transfer step. A quantitative description requires the use of quantum dynamical evolution as discussed in ref 26.

Acknowledgment. This research is supported by the Arnold and Mabel Beckman Foundation (SSI), the National Science Foundation, grant CHE-0750326 (SSI), and the National Institute of Health, grant GM-087475 (SSI). I.S. acknowledges support from the Kraft Fellowship and thanks G. A. Ferguson for helpful discussions.

References

- (1) Hynes, J. T.; Klinman, J. P.; Limbach, H.-H.; Schowen, R. L. *Hydrogen-Transfer Reactions*; Wiley-VCH: New York, 2007.
- (2) Isaacs, N. *Physical Organic Chemistry*; Wiley & Sons: New York, 1995.
- (3) Sheridan, R. *Quantum Mechanical Tunneling in Organic Reactive Intermediates*; Wiley-Interscience: Hoboken, NJ, 2007.
- (4) Bell, R. P. *The Proton in Chemistry*; Cornell University Press: Ithaca, NY, 1973.
- (5) Brunton, G.; Griller, D.; Barclay, L. R. C.; Ingold, K. U. *J. Am. Chem. Soc.* **1976**, *98*, 6803.
- (6) Nagel, Z.; Klinman, J. *Chem. Rev.* **2006**, *106* (8), 3095–3118.
- (7) Warshel, A. *Computer Modeling of Chemical Reactions in Enzymes and Solutions*; John Wiley & Sons, Inc.: New York, 1997.
- (8) Garcia-Viloca, M.; Gao, J.; Karplus, M.; Truhlar, D. G. *Science* **2004**, *303*, 5655.
- (9) Hammes-Schiffer, S.; Benkovic, S. J. *Ann. Rev. Biochem.* **2006**, *75*, 519.
- (10) Antoniou, D.; Basner, J.; Nunez, S.; Schwartz, S. *Chem. Rev.* **2006**, *106* (8), 3170–3187.
- (11) Cha, Y.; Murray, C. J.; Klinman, J. P. *Science* **1989**, *243*, 1325.
- (12) Bahnson, B. J.; Colby, T. D.; Chin, J. K.; Goldstein, B. M.; Klinman, J. P. *Proc. Natl. Acad. Sci. U.S.A.* **1997**, *94*, 12797.
- (13) Liang, Z. X.; Klinman, J. P. *Curr. Opin. Struct. Biol.* **2004**, *14*, 648.
- (14) Hwang, J.; Chu, Z.; Yadav, A.; Warshel, A. *J. Phys. Chem.* **1991**, *95* (22), 8445–8448.
- (15) Hwang, J. K.; Warshel, A. *J. Am. Chem. Soc.* **1996**, *118* (47), 11745–11751.
- (16) Olsson, M. H. M.; Siegbahn, P. E. M.; Warshel, A. *J. Am. Chem. Soc.* **2004**, *126*, 2820–2828.
- (17) Olsson, M. H. M.; Siegbahn, P. E. M.; Warshel, A. *J. Biol. Inorg. Chem.* **2004**, *9*, 96–99.
- (18) Mavri, J.; Liu, H.; Olsson, M. H. M.; Warshel, A. *J. Phys. Chem. B* **2008**, *112* (19), 5950–5954.
- (19) Olsson, M. H. M.; Mavri, J.; Warshel, A. *Phil. Tran. R. Soc. B* **2006**, *361*, 1417–1432.
- (20) Olsson, M. H. M.; Parson, W. W.; Warshel, A. *Chem. Rev.* **2006**, *106*, 1737–1756.
- (21) Liu, H.; Warshel, A. *J. Phys. Chem. B* **2007**, *111*, 7852–7861.
- (22) Pu, J. Z.; Gao, J. L.; Truhlar, D. G. *Chem. Rev.* **2006**, *106*, 3140–3169.
- (23) Hatcher, E.; Soudackov, A. V.; Hammes-Schiffer, S. *J. Am. Chem. Soc.* **2007**, *129*, 187.
- (24) Hatcher, E.; Soudackov, A. V.; Hammes-Schiffer, S. *J. Am. Chem. Soc.* **2004**, *126*, 5763–5775.

- (25) Siebrand, W.; Smedarchina, Z. *J. Phys. Chem. B* **2004**, *108*, 4185.
- (26) Iyengar, S. S.; Sumner, I.; Jakowski, J. *J. Phys. Chem. B* **2008**, *112*, 7601.
- (27) Dutton, P. L.; Munro, A. W.; Scrutton, N. S.; Sutcliffe, M. J. *Phil. Trans. R. Soc. London, Ser. B* **2006**, *361* (1472), 1293–1294.
- (28) Klinman, J. P. *Pure Appl. Chem.* **2003**, *75*, 601.
- (29) Glickman, M. H.; Wiseman, J. S.; Klinman, J. P. *J. Am. Chem. Soc.* **1994**, *116*, 793–794.
- (30) Antoniou, D.; Schwartz, S. D. *Proc. Natl. Acad. Sci.* **1997**, *94*, 12360–12365.
- (31) Lehnert, N.; Solomon, E. I. *J. Biol. Inorg. Chem.* **2003**, *8*, 294.
- (32) Tejero, I.; Garcia-Viloca, M.; Gonzalez-Lafont, A.; Lluch, J. M.; York, D. M. *J. Phys. Chem. B* **2006**, *110*, 24708.
- (33) Segraves, E. N.; Holman, T. R. *Biochemistry* **2003**, *42*, 5236–5243.
- (34) Garcia-Viloca, M.; Alhambra, C.; Truhlar, D. G.; Gao, J. L. *J. Comput. Chem.* **2003**, *24*, 177–190.
- (35) Billeter, S. R.; Webb, S. P.; Agarwal, P. K.; Iordanov, T.; Hammes-Schiffer, S. *J. Am. Chem. Soc.* **2001**, *123*, 11262–11272.
- (36) Warshel, A.; Sharma, P.; Kato, M.; Xiang, Y.; Liu, H.; Olsson, M. *Chem. Rev.* **2006**, *106* (8), 3210–3235.
- (37) Kuznetsov, A. M.; Ulstrup, J. *Can. J. Chem.—Rev. Can. Chim.* **1999**, *77*, 1085.
- (38) Meyer, M. P.; Klinman, J. P. *Chem. Phys.* **2005**, *319*, 283.
- (39) Gillan, M. J. *J. Phys. C* **1987**, *20*, 3621.
- (40) Voth, G. A.; Chandler, D.; Miller, W. H. *J. Chem. Phys.* **1989**, *91*, 7749.
- (41) Warshel, A.; Chu, Z. T. *J. Chem. Phys.* **1990**, *93*, 4003.
- (42) Warshel, A.; Weiss, R. M. *J. Am. Chem. Soc.* **1980**, *102*, 6218.
- (43) Chang, Y.-T.; Miller, W. H. *J. Phys. Chem.* **1990**, *94*, 5884.
- (44) Day, T. J. F.; Soudachov, A. V.; Cuma, M.; Schmidt, U. W.; Voth, G. A. *J. Chem. Phys.* **2002**, *117*, 5839.
- (45) Gao, J. *Acc. Chem. Res.* **1996**, *29*, 298.
- (46) Warshel, A.; Levitt, M. *J. Mol. Biol.* **1976**, *103*, 227.
- (47) Singh, B.; Kollman, P. A. *J. Comput. Chem.* **1986**, *7*, 718.
- (48) Field, C.; Bash, P. A.; Karplus, M. *J. Comput. Chem.* **1990**, *11*, 700.
- (49) Benkovic, S. J.; Hammes-Schiffer, S. *Science* **2006**, *312*, 208.
- (50) Miller, W. H.; Schwartz, S. D.; Tromp, J. W. *J. Chem. Phys.* **1983**, *79*, 4889.
- (51) Iyengar, S. S.; Jakowski, J. *J. Chem. Phys.* **2005**, *122*, 114105.
- (52) Iyengar, S. S. *Theo. Chem. Accts.* **2006**, *116*, 326.
- (53) Jakowski, J.; Sumner, I.; Iyengar, S. S. *J. Chem. Theory Comput.* **2006**, *2*, 1203–1219.
- (54) Sumner, I.; Iyengar, S. S. *J. Phys. Chem. A* **2007**, *111*, 10313–10324.
- (55) Sumner, I.; Iyengar, S. S. *J. Chem. Phys.* **2008**, *129*, 054109.
- (56) Hoffman, D. K.; Nayar, N.; Sharafeddin, O. A.; Kouri, D. J. *J. Phys. Chem.* **1991**, *95*, 8299.
- (57) Kouri, D. J.; Huang, Y.; Hoffman, D. K. *Phys. Rev. Lett.* **1995**, *75*, 49–52.
- (58) Blomberg, M.; Siegbahn, P. *J. Phys. Chem. B* **2001**, *105* (39), 9375–9386.
- (59) Shuang, F.; Pechen, A.; Ho, T.; Rabitz, H. *J. Chem. Phys.* **2007**, *126*, 134303.
- (60) Tannor, D. J.; Rice, S. A. *J. Chem. Phys.* **1985**, *83* (10), 5013–5018.
- (61) Brumer, P.; Shapiro, M. *Acc. Chem. Res.* **1989**, *22* (12), 407–413.
- (62) Sakurai, J. J. *Modern Quantum Mechanics*; Addison-Wesley Publishing Company: Reading, MA, 1994.
- (63) Wheeler, J. A.; Zurek, W. H. Princeton University Press: Princeton, NJ, 1983.
- (64) Roa, L.; Delgado, A.; Ladron de Guevara, M. L.; Klimov, A. B. *Phys. Rev. A* **2006**, *73*, 012322.
- (65) Roa, L.; Olivares-Renteria, G. A. *Phys. Rev. A* **2006**, *73*, 062327.
- (66) Roa, L.; Olivares-Renteria, G. A.; de Guevara, M. L. L.; Delgado, A. *Phys. Rev. A* **2007**, *75*, 014303.
- (67) Pechen, A.; Il'in, N.; Shuang, F.; Rabitz, H. *Phys. Rev. A* **2006**, *74*, 052102.
- (68) Shuang, F.; Zhou, M.; Pechen, A.; Wu, R.; Shir, O. M.; Rabitz, H. *Phys. Rev. A* **2008**, *78*, 063422.
- (69) Prezhdo, O. V. *Phys. Rev. Lett.* **2000**, *85*, 4413.
- (70) Jacobs, K.; Steck, D. A. *Contemp. Phys.* **2006**, *47* (5), 279–303.
- (71) Diosi, L.; Halliwell, J. J. *Phys. Rev. Lett.* **1998**, *81* (14), 2846.
- (72) Halliwell, J. J. *Int. J. Theor. Phys.* **1999**, *38* (11), 2969.
- (73) Brun, T. A. *Am. J. Phys.* **2002**, *70* (7), 719.
- (74) Mensky, M. *Phys. Lett. A* **1994**, *196*, 159–167.
- (75) Mensky, M. B. *Phys. Lett. A* **2003**, *307*, 85–92.
- (76) Tannor, D. J. *Introduction to Quantum Mechanics: A Time-dependent Perspective*; University Science Books: New York, 2007.
- (77) Feynman, R. P.; Vernon, F. L.; Hellwarth, R. W. *J. Appl. Phys.* **1957**, *28*, 49.
- (78) Sorensen, D. C. *SIAM J. Matr. Anal. Apps.* **1992**, *13*, 357–385.
- (79) Golub, G. H.; van Loan, C. F. *Matrix Computations*; The Johns Hopkins University Press: Baltimore, MD, 1996.
- (80) Knapp, M. J.; Rickert, K.; Klinman, J. P. *J. Am. Chem. Soc.* **2002**, *124*, 3865.
- (81) Hay, S.; Scrutton, N. S. *Biochemistry* **2008**, *47*, 9880–9887.
- (82) Meyer, M. P.; Tomchick, D. R.; Klinman, J. P. *Proc. Natl. Acad. Sci., U. S. A.* **2008**, *105*, 1146.
- (83) Schenk, G.; Neidig, M.; Zhou, J.; Holman, T.; Solomon, E. *Biochemistry* **2003**, *42* (24), 7294–7302.
- (84) Modi, K.; Shaji, A. *Phys. Lett. A* **2007**, *368*, 215–221.
- (85) Fischer, M. C.; Gutierrez-Medina, B.; Raizen, M. G. *Phys. Rev. Lett.* **2001**, *87*, 040402.